

# Nanoscale Elemental Sensitivity Study of Nd<sub>2</sub>Fe<sub>14</sub>B Using Absorption Correlation Tomography

THOMAS L. KAO,<sup>1</sup> CRYSTAL Y. SHI,<sup>2</sup> JUNYUE WANG,<sup>3,4</sup> WENDY L. MAO,<sup>2,5,6</sup> YIJIN LIU,<sup>7\*</sup> AND WENGE YANG<sup>3,4\*</sup>

<sup>1</sup>Palo Alto High School, Palo Alto, California 94301

<sup>2</sup>Geological and Environmental Sciences, Stanford University, Stanford, California 94305

<sup>3</sup>High Pressure Synergetic Consortium, Geophysical Laboratory, Carnegie Institution of Washington, Argonne, Illinois 60439

<sup>4</sup>Center for High Pressure Science and Technology Advanced Research, 1690 Cailun Rd, Pudong, Shanghai 201203, P.R. China

<sup>5</sup>Stanford Institute for Materials and Energy Sciences, SLAC National Accelerator Laboratory, California 94025

<sup>6</sup>Photon Science, SLAC National Accelerator Laboratory, California 94025

<sup>7</sup>Stanford Synchrotron Radiation Lightsource, SLAC National Accelerator Laboratory, California 94025

**KEY WORDS** transmission X-ray microscopy; synchrotron; absorption correlation

**ABSTRACT** Transmission X-ray microscopy (TXM) is a rapidly developing technique with the capability of nanoscale three dimensional (3D) real-space imaging. Combined with the wide range in energy tunability from synchrotron sources, TXM enables the retrieval of 3D microstructural information with elemental/chemical sensitivity that would otherwise be inaccessible. The differential absorption contrast above and below absorption edges has been used to reconstruct the distributions of different elements, assuming the absorption edges of the interested elements are fairly well separated. Here we present an “Absorption Correlation Tomography” (ACT) method based on the correlation of the material absorption across multiple edges. ACT overcomes the significant limitation caused by overlapping absorption edges, significantly expands the capabilities of TXM, and makes it possible for fully quantitative nano-scale 3D structural investigation with chemical/elemental sensitivity. The capability and robustness of this new methodology is demonstrated in a case study of an important type of rare earth magnet (Nd<sub>2</sub>Fe<sub>14</sub>B). *Microsc. Res. Tech.* 76:1112–1117, 2013. © 2013 Wiley Periodicals, Inc.

## INTRODUCTION

This past decade has seen revolutionary developments in X-ray imaging. The most substantial advances in this field are closely related to the availability of new generations of X-ray sources (synchrotrons and/or free electron lasers) and advanced X-ray optics. The outstanding brilliance and stability of the new X-ray sources has dramatically improved imaging speed and image quality leading to diverse applications ranging from biomedical research (Stampanoni et al., 2011) to the study of aerospace materials (Brennan, 2010; Stevenson et al., 2003). The development of nano-precision technologies has made the fabrication of fine scale X-ray optics, such as capillary condensers and Fresnel Zone plates (Yun et al., 1999; Zeng et al., 2008), for focusing the beam and for being used as objective lens respectively, mitigating the limitations in imaging resolution set by microscope hardware. Optical analyzers [such as single crystals (Chapman et al., 1997), grating interferometers (Zhu et al., 2010), and phase rings (Andrews et al., 2011)] have been employed for extracting the information that is related to different interactions between the X-rays and the specimen (e.g., the scattering, the beam divergence, and the phase shift) (Oltulu et al., 2003; Pfeiffer et al., 2008).

In conjunction with developments in nano-focusing X-ray optics, another important development is related to taking the advantage of the energy tunability of synchrotron X-ray sources. X-ray spectroscopy is well recognized as a powerful tool for the element specific

characterization of materials. The combination of X-ray microscopy and X-ray spectroscopy makes it possible to investigate compositional information along with the 3D structure of the sample. The main challenge is the ability to conduct spatially resolved spectroscopic measurements at very fine length scales (down to a few tens of nanometers). By carrying out a raster scan of the sample and collecting the desired information pixel by pixel, 2D chemical maps can be generated using scanning transmission X-ray microscopy (STXM), which has dominated this field for a considerable time (Williams et al., 1995), although wider use of this technique has been limited due to the long data collection time required. Equipping Fresnel zone plates as magnifying lens in full-field TXM (Andrews et al., 2010; Yuan et al., 2012; Chu et al., 2008; Wang et al., 2012a) makes it a very promising technique for conducting fast 3D imaging with chemical/elemental sensitivity by implementing energy scans over absorption edges of the elements of interest and tomography

\*Correspondence to: Yijin Liu, Stanford Synchrotron Radiation Lightsource, SLAC National Accelerator Laboratory, California 94025, USA. E-mail: liuyijin@slac.stanford.edu or Wenge Yang, High Pressure Synergetic Consortium, Geophysical Laboratory, Carnegie Institution of Washington, Argonne, Illinois 60439, USA. E-mail: wyang@ciw.edu

Received 6 May 2013; accepted in revised form 13 July 2013  
Additional Supporting Information may be found in the online version of this article.

Contract grant sponsor: NIH/NIBIB; Contract grant number: 5R01EB004321; Contract grant sponsor: DOE-BES; Contract grant number: DE-SC 0001057.

DOI 10.1002/jemt.22273

Published online 6 August 2013 in Wiley Online Library (wileyonlinelibrary.com).

scans in TXM (Liu et al., 2012b; Meirer et al., 2011; Rau et al., 2003).

One important technical difficulty that needs to be addressed for conducting energy resolved TXM is that the focal length of the objective zone plate is actually a function of the X-ray energy, complicating the data acquisition and/or analysis. Different ideas have been investigated to avoid/compensate for this effect. From the experimental side, three main methods have been proposed: (1) choosing a combination of energy points that result in the same magnification (Yin et al., 2006); (2) recording images at two energy points that are very close to each other (Grew et al., 2010); and (3) adjusting the position of the zone plate and the detector simultaneously as the energy is scanned in order to keep the magnification constant (Wang et al., 2012a). From the data manipulation side, algorithms for image correction/registration have also been introduced (Liu et al., 2012b). However, all of these methods rely on the assumption that the absorption edges of all the elements of interest are fairly well separated, which is not always true in many samples. It is clear that a method that can extract the elemental distribution in materials despite the presence of overlapping absorption edges would be a scientific breakthrough enabling fully quantitative 3D structural study with chemical/elemental sensitivity.

Here we propose a novel approach for performing nanoscale TXM imaging that quantitatively reconstructs the 3D structure with chemical/elemental sensitivity in samples with (and without) overlapping absorption edges. The method, which we call absorption correlation tomography (ACT) utilizes previously undescribed analyses of the correlation between X-ray absorption at different edges with no additional constraint (such as coherence) compared to the previously proposed TXM methods for obtaining chemical/elemental specific structural information. We apply this approach for the first time to the rare earth magnet system Nd<sub>2</sub>Fe<sub>14</sub>B, in which the Nd L1-edge overlaps the Fe K-edge, to nondestructively reveal the 3D distribution of chemical inhomogeneity in the sample with 30-nm spatial resolution, which provides important microstructure analysis for manufacturers to improve performance for the next generation of energy materials.

## METHODS

The innovative approach presented here relies on the fact that a certain element has multiple absorption edges accessible by TXM. An absorption edge results when the core electrons absorb photons whose energies are greater than or equal to their binding energies. Most elements have multiple core electrons and, therefore multiple steep rises of the absorption coefficient at the core-level binding energies of different electrons. The amount of the rise in absorption coefficient at a certain absorption edge is proportional to the number of targeted atoms probed and thus to the concentration of the element. There is a linear correlation among different edges of the same element, which is the key factor exploited by the methodology proposed in this article. When overlapping edges are present, the linearity of the correlation degrades on account of the contribution from another edge of a different element. We

propose to use the covariance of the edge jumps [ $JmpCov$ , as defined in Eq. (1)] as a pragmatic parameter for semi-quantitative analysis of the degree of contamination by the other element.

$$\begin{aligned} JmpCov &= Cov\left(\mu \left| \begin{matrix} En_{H_1} \\ En_{L_1} \end{matrix} \right., \mu \left| \begin{matrix} En_{H_2} \\ En_{L_2} \end{matrix} \right.\right) \\ &= E\left[\left(\mu \left| \begin{matrix} En_{H_1} \\ En_{L_1} \end{matrix} \right. - E\left[\mu \left| \begin{matrix} En_{H_1} \\ En_{L_1} \end{matrix} \right.\right]\right)\left(\mu \left| \begin{matrix} En_{H_2} \\ En_{L_2} \end{matrix} \right. - E\left[\mu \left| \begin{matrix} En_{H_2} \\ En_{L_2} \end{matrix} \right.\right]\right)\right] \end{aligned} \quad (1)$$

In Eq. (1),  $Cov$  denotes the covariance function;  $E$  denotes the function of calculating expectation value;  $\mu$  is the absorption coefficient which is typically 3D matrices of size approximately  $1k \times 1k \times 1k$  in our case;  $En_{H_1}$  and  $En_{H_2}$  are the two energies above the two absorption edges;  $En_{L_1}$  and  $En_{L_2}$  are the two energies below the corresponding absorption edges. A material without any overlapping edges would give  $JmpCov$  proportional to the variance of the distribution of either of the two edge jumps. This value will decrease when overlapping edges occur, indicating the ‘‘contamination.’’

Further quantification for separating the contribution from the two elements is based on analyzing the ratio between the edge jumps. The distribution of the polar angle in the correlation plot [ $JmpPolarAng$ , as defined in Eq. (2)] contains information about the relative concentration of the two elements involved.

$$JmpPolarAng = \text{atan}\left(\mu \left| \begin{matrix} En_{H_2} \\ En_{L_2} \end{matrix} \right. / \mu \left| \begin{matrix} En_{H_1} \\ En_{L_1} \end{matrix} \right.\right) \quad (2)$$

## RESULTS

For our first case study, we chose the well-studied permanent magnet system (Nd<sub>2</sub>Fe<sub>14</sub>B). Since the discovery of the Nd<sub>2</sub>Fe<sub>14</sub>B compound by general motors and Sumitomo special metal in 1982 (Herbst et al., 1984), this system has been the subject of numerous fundamental and applied studies. As the most widely used and strongest type of rare-earth permanent magnet system, Nd<sub>2</sub>Fe<sub>14</sub>B has many important industrial applications [e.g., in high density magnetic recording (Kryder et al., 2008), MRI scanners (Jiang et al., 2004), Maglev (US Dep. Transportation, 2003), electric vehicles (Wang et al., 2008), etc.]. Continuous and considerable effort to improve the performance (e.g., the magnetism, thermal stability, coercivity, etc.) of neodymium magnets has been made, with one of the most widely adapted methods for improving the magnetic properties being the substitution of other element(s). A critical aspect for understanding the mechanism behind the functionality of this material is to determine the alloy composition and microstructure over a representative volume of the sample. It is especially important to be able to characterize the degree of homogeneity/heterogeneity in a sample at different length scales when substitution of various metals is applied.

We studied a small piece of Nd<sub>2</sub>Fe<sub>14</sub>B crushed from a magnet rod (Goodfellow, item #531-114-16).

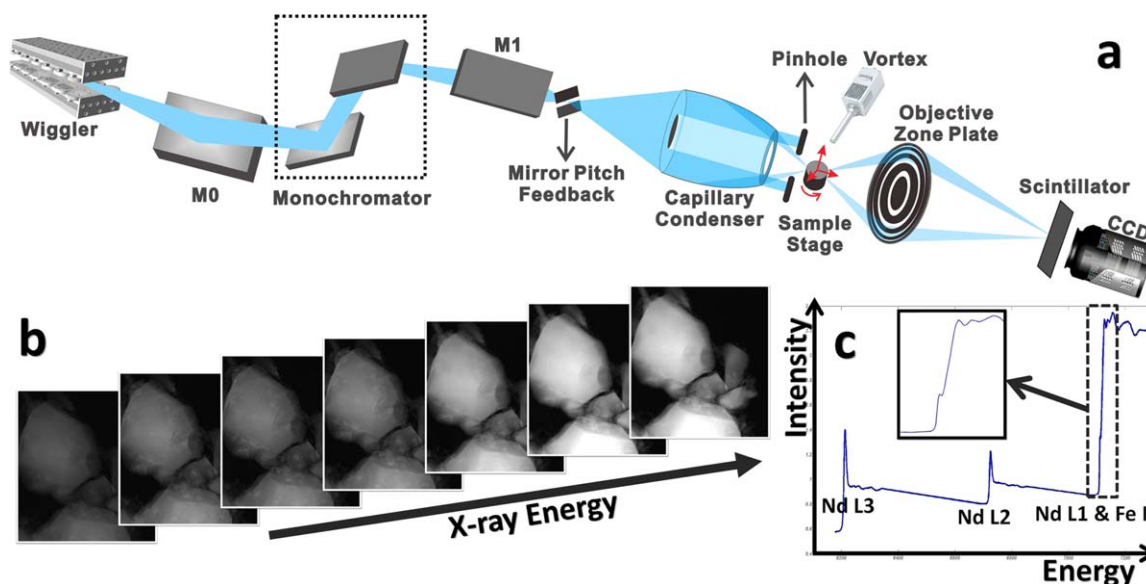


Fig. 1. (a) Schematic of the TXM installed at beamline 6-2C of SSRL. The wide smooth energy spectrum of a wiggler source and high stability of the monochromator provides the energy tunability, and the high precision (translation and rotation) sample stage and dedicated objective zone plate enable nanoscale 3D tomography. The off-axis vortex detector is used to confirm elemental fluorescence lines. (b) Series of 2D transmission images from the  $\text{Nd}_2\text{Fe}_{14}\text{B}$  sample

with incident X-ray energy across 3 L-edges of Nd and the K-edge of Fe, demonstrating the fact that the absorption coefficient of the studied ROI changes as a function of the energy. (c) Plot of the averaged intensity over the entire FOV as a function of the energy. The magnified plot in (c) shows the overlapping region of the Fe K and the Nd  $L_1$  edges. [Color figure can be viewed in the online issue, which is available at [wileyonlinelibrary.com](http://wileyonlinelibrary.com).]

A schematic of the experiment is shown in Figure 1. The projected images of the selected magnet particles were collected using the TXM (Fig. 1a) installed at Beamline 6-2C of the Stanford Synchrotron Radiation Lightsource (SSRL) (Andrews et al., 2010). An off-axis VORTEX Silicon Drift detector was used to verify the presence of the elements of interest (Nd and Fe) by checking the fluorescence peaks from the X-ray illuminated region (typically about  $30 \times 30 \mu\text{m}^2$ ) (Liu et al., 2012a). The 2D TXM absorption images were collected with the incident X-ray energy scan (Fig. 1b). From each region of interest (ROI), one can plot the absorption coefficient profile of the material as a function of the incident X-ray energy (Fig. 1c).

To avoid chemical bonding related absorption coefficient features near the absorption edge, we chose incident energies 50 eV above and below the Nd L edges and Fe K edge. Tomography data were collected at multiple X-ray energies (at 6158, 6258, 6672, 6772, 7062, and 7176 eV) with a half degree angular step from  $0^\circ$  to  $180^\circ$  to obtain the distribution of edge jumps with 3D spatial resolution down to around 30 nm. Difference maps between images taken above and below the Nd  $L_2$  edge (at 6722 eV) and the Nd  $L_3$  edge (at 6208 eV), and those between the images taken at 7062 and 7176 eV were generated using the TXM-Wizard software package (Liu et al., 2012b).

As illustrated in Figure 1c, the Nd  $L_1$  edge (7126 eV) and the Fe K edge (7112) are so close to each other that the  $\pm 50$  eV absorption contrast from these edges will include both elements which presents a challenge for the quantitative study of the distribution of Nd and Fe in this sample. The proposed edge jump covariance method (see online method section) is the ideal approach to solve this problem.

An iterative tomography reconstruction algorithm (Wang et al., 2012b) was adapted for the reconstruction of the three sets of difference maps from the tomography data collected at six energies, resulting in three of the 3D matrices of edge jump amplitudes. The correlation between the edge jump of the Nd  $L_2$  edge and that of the Nd  $L_3$  edge is plotted in Figure 2a; and the one between the edge jump of the Nd  $L_3$  edge and that of the overlapping Fe K edge and Nd  $L_1$  edge is shown in Figure 2b.

As expected, Figure 2a shows strong linear correlation between the edge jump for the Nd  $L_3$  and that of the Nd  $L_2$  edges. This is because both of these edge jumps represent the distribution of Nd only in the sample. The situation is more complicated in Figure 2b. The horizontal axis ( $\mu_{7176}-\mu_{7062}$ ) contains contributions from both the edge jump of the Nd  $L_1$  edge and that of the Fe K edge, while the vertical axis only shows the contribution from the Nd  $L_3$  edge jump. From Figure 2b, one can see that there are three distinct groups, indicating that there are three main components with different Nd/Fe ratios present in the studied particle. The difference between the absorption coefficients at 7176 and 7062 eV is proportional to the total amount of Nd and Fe; while the polar angle of each data point in Figure 2b denotes the relative concentration of these two elements for the corresponding voxel in the 3D matrix. For further quantitative analysis, the histogram of the polar angles of the data points in Figure 2b is plotted in Figure 2c. It worth mentioning that most of the voxels give Fe/Nd atomic ratios between 6:1 and 8:1, as shown in the green-shaded area in Figure 2c, indicating that  $\text{Nd}_2\text{Fe}_{14}\text{B}$  is the dominant phase in the investigated particle but with considerable variation of the chemical composition. The

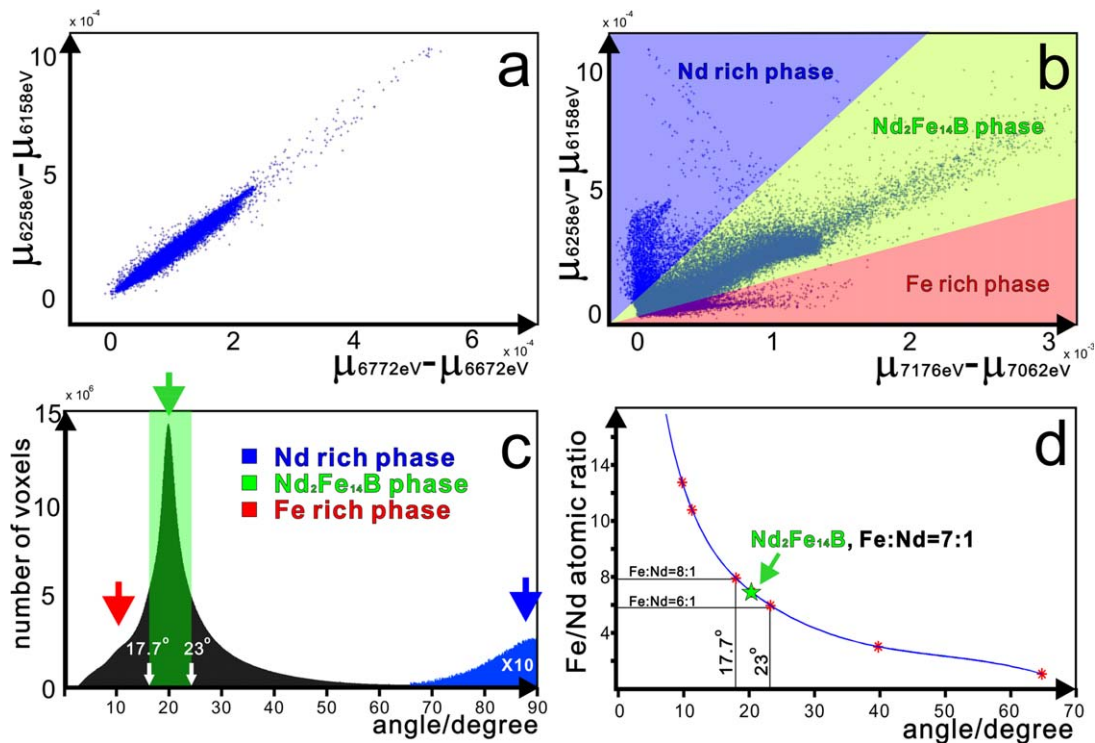


Fig. 2. (a) The correlation between the edge jump of the Nd L<sub>1</sub> edge and that of the Nd L<sub>2</sub> edge. (b) The correlation between the edge jump of the Nd L<sub>3</sub> and that of the overlapping Nd L<sub>1</sub> edge and Fe K edge. The result in (b) can be separated into three distinct groups, indicating that there are three main components (with different Nd/Fe ratios) present in the material. (c) Histogram plot of the polar

angles of the data points in panel b. The plot for the Nd rich phase was magnified by a factor of 10 for better visualization. The green-shaded area represents the Fe/Nd atomic ratios between 8:1 and 6:1, as indicated in panel (d), which is the calculated plot of Fe/Nd atomic ratio as a function of the polar angle. [Color figure can be viewed in the online issue, which is available at [wileyonlinelibrary.com](http://wileyonlinelibrary.com).]

calculated relationship of the Fe/Nd atomic ratio to the polar angle is plotted in Figure 2d.

Taking the Nd/Fe ratio retrieved from the polar angles of the data points in the correlation plot (Fig. 2b) into consideration, the total amount of edge jump between the absorption coefficients at 7176 and 7062 eV can be separated into two parts (the contribution from the Fe K edge and the contribution from Nd L<sub>1</sub> edge). As a result, the 3D distribution of Fe and Nd can be retrieved quantitatively, and are displayed with two sets of slices through different depths of the studied volume (Figs. 3a–3f). As indicated by the selected ROI in Figure 3a through Figure 3f, segregation of Nd at submicron scales is observed both inside and on the surface of the particles. The corresponding Nd/Fe ratio maps are also demonstrated in Figures 3g–3i, with a magnified and rescaled view of a selected area of Figure 3h. The Nd-rich layer at the surface and the nanopattern of the heterogeneity are clearly visible in the mesh view of the Nd/Fe ratio maps.

The merged 3D rendering for both the Nd and Fe distributions is demonstrated in Figure 4a with two magnified views of the selected ROIs shown in Figures 4b and 4c. From both the 2D sections and 3D magnified views, one can clearly see the inhomogeneity of Nd/Fe distribution. The observed pure Nd rod inside the magnet could produce a magnetic pinning effect which may prevent the alignment of local magnetic domains, while the excess Nd on the surface also modi-

fies the repulsive/attractive forces between adjacent particles.

## DISCUSSION

The 3D nanoscale morphology and elemental specific composite distribution in the Nd<sub>2</sub>Fe<sub>14</sub>B material represents important information about this magnetic material. The results provided by the novel ACT method demonstrate its potential for improved characterization and understanding of nanocomposite magnets prepared by various methods, including melt spinning, mechanical milling, sputtering and chemical synthesis. Coupled with other techniques such as resistive and laser heating and compression in diamond anvil cells, it offers the capability for studying the effects of heat treatment and changes in materials properties under extreme environments (Wang et al., 2012b). The combination of full-field X-ray imaging and X-ray energy-tuning capability also provides the possibility of X-ray spectroscopic analysis with 3D spatial resolution down to  $30 \times 30 \times 30 \text{ nm}^3$ .

The 3D elemental distribution of Nd<sub>2</sub>Fe<sub>14</sub>B particles was determined quantitatively using synchrotron-based full-field TXM. By analyzing the correlation between the edge jumps of the material at different absorption edges, the ACT method proposed in this letter overcomes the difficulty in retrieving the distribution of different elements in 3D caused by the overlap of absorption edges. The presented method can provide

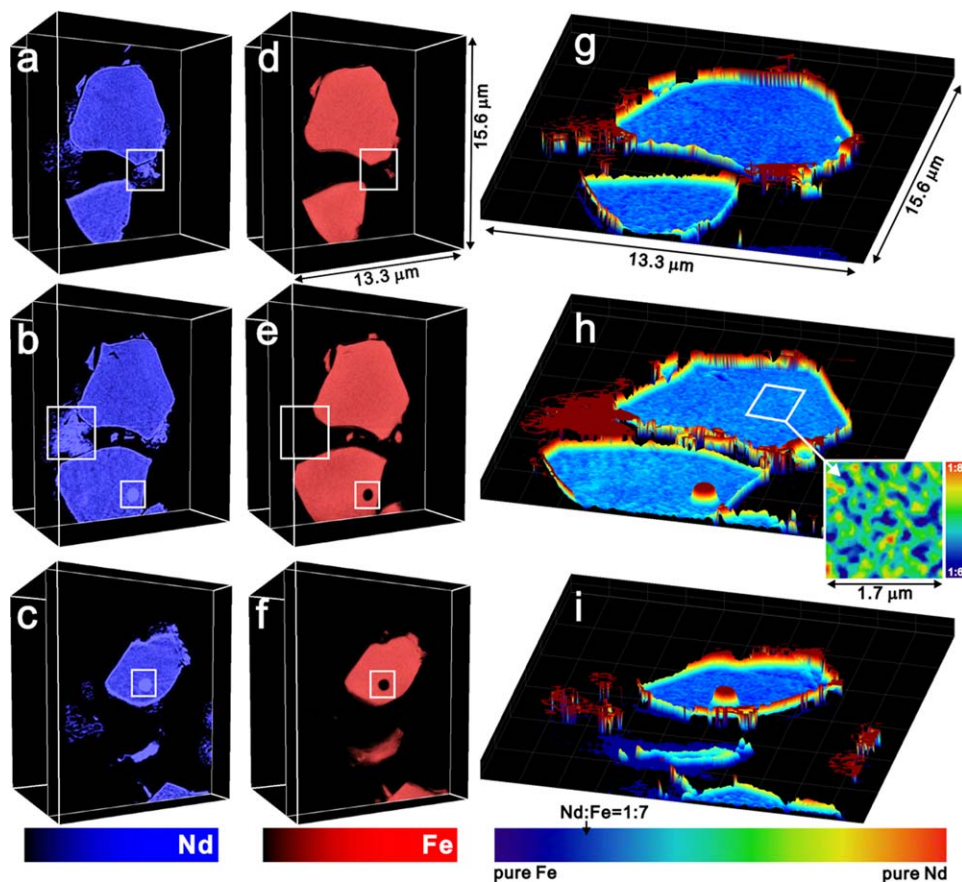


Fig. 3. The 3D distributions of Fe and Nd. Panels (a) through (c) are slices of Nd distribution through different depths in the studied volume; panels (d) through (f) are the corresponding slices for Fe distribution. It can be seen in the outlined regions of interest that the distribution of Fe and Nd are of considerable difference. The mesh view of the Nd/Fe ratio maps are shown in panels (g) to (i), with a

magnified and rescaled view of the selected region in panel h). The color at the right of each color map on the bottom represents higher concentrations of the corresponding elements or higher Nd/Fe ratio. [Color figure can be viewed in the online issue, which is available at wileyonlinelibrary.com.]

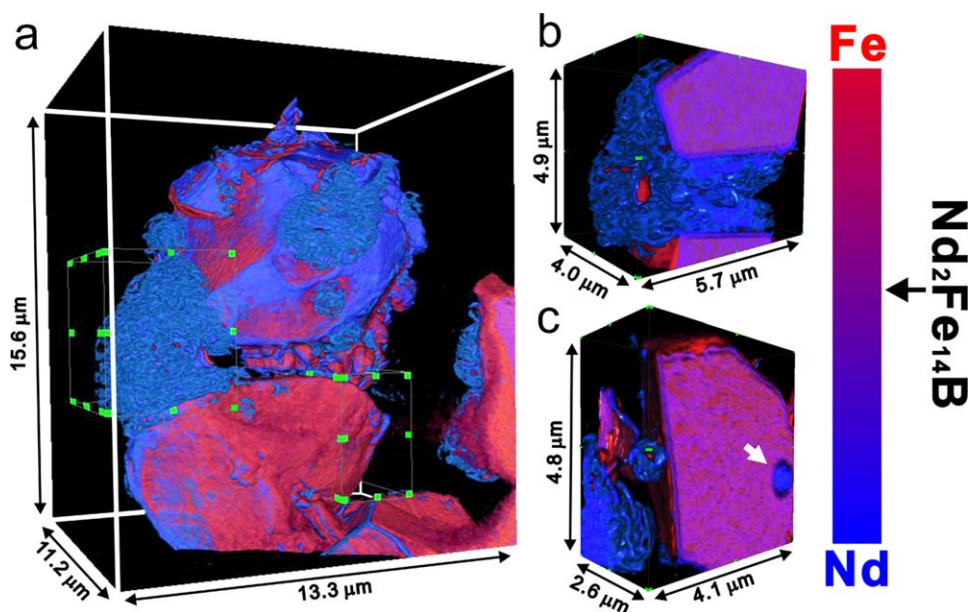


Fig. 4. (a) Merged 3D rendering of the distribution of Nd (in blue) and Fe (in red). (b) and (c) are the magnified views of the selected regions of interest indicated in panel a), but viewing from inside of the particle to outside. The color legend represents the continuous composition change from Fe rich to Nd rich. The arrow in the color legend points to the ideal Fe/Nd ratio of 7:1. Excess Nd at the surface

and between two particles, and the internal Nd-rich rod (indicated with the arrow in panel c) can be clearly seen from the ACT data analysis, while isolated Fe rich regions near the surface and inside the particle are present. The movie of the rendering can be found in the Supporting Information file. [Color figure can be viewed in the online issue, which is available at wileyonlinelibrary.com.]

important insights into the microstructure and chemical composition inhomogeneity studies of multi-element systems in biology, environmental, and materials science research.

#### AUTHOR CONTRIBUTIONS

Y.L. and W.Y. designed the project; T.L.K., C.Y.S., J.W., Y.L., and W.Y. performed the experiments; T.L.K., W.L.M., Y.L., and W.Y. wrote the paper; T.L.K., Y.L., and W.Y. analyzed the data. All the authors read and commented on the manuscript.

#### ACKNOWLEDGMENTS

The authors gratefully thank Dr. Joy C. Andrews (SLAC), Dr. Johanna Nelson (SLAC), and the staffs at Carl Zeiss X-ray Microscopy for helpful discussions.

#### REFERENCES

- Andrews JC, Almeida E, van der Meulen MC, Alwood JS, Lee C, Liu Y, Chen J, Meirer F, Feser M, Gelb J, Rudati J, Tkachuk A, Yun W, Pianetta P. 2010. Nanoscale X-ray microscopic imaging of mammalian mineralized tissue. *J Microsc Microanal* 16:327–336.
- Andrews JC, Meirer F, Liu Y, Mester Z, Pianetta P. 2011. Transmission X-ray microscopy for full-field nano imaging of biomaterials. *Microsc Res Tech* 74:671–681.
- Brennan S. 2010. Astromaterials research of comet wild 2: Tetrameters to nanometers. *MRS Bull* 35:150–154.
- Chapman D, Thomlinson W, Johnston RE, Washburn D, Pisano E, Gmür N, Zhong Z, Menk R, Arfelli F, Sayers D. 1997. Diffraction enhanced X-ray imaging. *Phys Med Biol* 42:2015.
- Chu YS, Yi JM, De Carlo F, Shen Q, Lee WK, Wu HJ, Wang CL, Wang JY, Liu CJ, Wang CH, Wu SR, Chien CC, Hwu Y, Tkachuk A, Yun W, Feser M, Liang KS, Yang CS, Je JH, Margaritondo G. 2008. Hard-x-ray microscopy with Fresnel zone plates reaches 40 nm Rayleigh resolution. *Appl Phys Lett* 92:103119.
- Grew KN, Chu YS, Yi J, Peracchio AA, Izzo JR Jr, Hwu Y, De Carlo F, Chiu WKS. 2010. Nondestructive nanoscale 3D elemental mapping and analysis of a solid oxide fuel cell anode. *J Electrochem Soc* 157:783–792.
- Herbst JF, Croat JJ, Pinkerton FE, Yelon WB. 1984. Relationships between crystal structure and magnetic properties in Nd<sub>2</sub>Fe<sub>14</sub>B. *Phys Rev B* 29:4176–4178.
- Jiang X, Shen G, Lai Y, Tian J. 2004. Development of an open 0.3 T NdFeB MRI magnet. *Appl Supercond IEEE Trans* 14:1621–1623.
- Kryder MH, Gage EC, McDaniel TW, Challener WA, Rottmayer RE, Ju G, Hsia YT, Erden MF. 2008. Heat assisted magnetic recording. *Proc IEEE* 96:1810–1835.
- Liu Y, Meirer F, Wang J, Requena G, Williams P, Nelson J, Mehta A, Andrews JC, Pianetta P. 2012a. 3D elemental sensitive imaging using transmission X-ray microscopy. *Anal Bioanal Chem* 404:1297–1301.
- Liu Y, Meirer F, Williams PA, Wang J, Andrews JC, Pianetta P. 2012b. TXM-Wizard: A program for advantage data collection and evaluation in full-field transmission X-ray microscopy. *J Synchrotron Rad* 19:281–287.
- Meirer F, Cabana J, Liu Y, Mehta A, Andrews JC, Pianetta P. 2011. Three-dimensional imaging of chemical phase transformations at the nanoscale with full-field transmission X-ray microscopy. *J Synchrotron Rad* 18:773–781.
- Oltulu O, Zhong Z, Hasnah M, Wernick MN, Chapman D. 2003. Extraction of extinction, refraction and absorption properties in diffraction enhanced imaging. *J Phys D Appl Phys* 36:2152–2156.
- Pfeiffer F, Bech M, Bunk O, Kraft P, Eikenberry EF, Brönnimann CH, Grünzweig C, David C. 2008. Hard-X-ray dark-field imaging using a grating interferometer. *Nat Mater* 7:134–137.
- Rau C, Somogyi A, Simionovici A. 2003. Microimaging and tomography with chemical speciation. *Nucl Instr Meth Phys Res B* 200:444–450.
- Stampanoni M, Wang Z, Thuring T, David C, Roessl E, Trippel M, Singer G, Hohl MK, Hauser N. 2011. The first analysis and clinical evaluation of native breast tissue using differential phase-contrast mammography. *Invest Radiol* 46:801–806.
- Stevenson AW, Gureyev TE, Paganin D, Wilkins SW, Weitkamp T, Snigireva I, Youn HS, Dolbnya IP, Yun W, Lai B, Garrett RF, Cookson DJ, Hyodo K, Ando M. 2003. Phase-contrast X-ray imaging with synchrotron radiation for materials science applications. *Nucl Instr Meth In Phys Res B* 199:427–435.
- US Department of Transportation. 2003. Federal Transit Administration, The M3 urban maglev system. FTA Project Rep MA-26-7077.
- Wang A, Li H, Liu C. 2008. On the material and temperature impacts of interior permanent magnet machine for electric vehicle applications. *IEEE Trans Magn* 44:4329–4332.
- Wang J, Chen YK, Yuan Q, Tkachuk A, Erdonmez C, Hornberger B, Feser M. 2012a. Automated markerless full field hard X-ray microscopic tomography at sub-50 nm 3-dimension spatial resolution. *Appl Phys Lett* 100:143107.
- Wang J, Yang W, Wang S, Xiao X, De Carlo F, Liu Y, Mao WL. 2012b. High pressure nano-tomography using an iterative method. *J Appl Phys* 111:112626.
- Williams S, Jacobsen C, Kirz J, Maser J, Wirick S, Zhang X, Ade H, Rivers M. 1995. Instrumentation developments in scanning soft x-ray microscopy at the NSLS. *Rev Sci Instrum* 66:1271–1275.
- Yin GC, Tang MT, Song YF, Chen FR, Liang KS, Diewer FW, Yun W, Ko CH, Shieh HPD. 2006. Energy-tunable transmission X-ray microscope for differential contrast imaging with near 60 nm resolution tomography. *Appl Phys Lett* 88:24115.
- Yuan Q, Zhang K, Hong Y, Huang W, Gao K, Wang Z, Zhu P, Gelb J, Tkachuk A, Hornberger B, Feser M, Yun W, Wu Z. 2012. A 30 nm-resolution hard X-ray microscope with X-ray fluorescence mapping capability at BSRF. *J Synchrotron Rad* 19:1021–1028.
- Yun W, Lai B, Cai Z, Maser J, Legnini D, Gluskin E, Chen Z, Krasnoperova AA, Vladimirovsky Y, Cerrina F, Di Fabrizio E, Gentili M. 1999. Nanometer focusing of hard X rays by phase zone plates. *Rev Sci Instrum* 70:2238–2241.
- Zeng X, Diewer F, Feser M, Huang C, Lyon A, Tkachuk A, Yun W. 2008. Ellipsoidal and parabolic glass capillaries as condensers for X-ray microscopes. *Appl Opt* 47:2376–2381.
- Zhu P, Zhang K, Wang Z, Liu Y, Liu X, Wu Z, McDonald SA, Marone F, Stampanoni M. 2010. Low-dose, simple, and fast grating-based X-ray phase-contrast imaging. *Proc Natl Acad Sci USA* 107:13576.